

# Epidermal homeostasis control in an off-lattice agent-based model

Gernot Schaller and Michael Meyer-Hermann

*Frankfurt Institute for Advanced Studies (FIAS), Johann Wolfgang Goethe-Universität,  
Max von Laue-Straße 1, D-60438 Frankfurt am Main, Germany\**

(Dated: May 24, 2019)

We apply an improved version of a previously introduced off-lattice agent-based model to the steady-state flow equilibrium of skin. The dynamics of cells is determined by conservative and drag forces, supplemented with delta-correlated random forces. Cellular adjacency is detected by a weighted Delaunay triangulation. We analyze a simple control mechanism: The cell cycle time of keratinocytes is controlled by a diffusible substance provided by the dermis, in particular we consider the local water concentration. This concentration is calculated from a diffusion equation with time-dependent boundary conditions and varying diffusion coefficients. It turns out that this simple control mechanism suffices to explain several characteristics of epidermal growth. The dynamics of a nutrient is also taken into account by a reaction-diffusion equation. In addition, we ask the simple question of how melanoma with decreased basal adhesion manage to persist within the steady-state flow-equilibrium of the skin. It turns out that there exist physiological parameter sets, where stochastic effects have important consequences.

Keywords: Delaunay triangulation, epidermis, melanoma, adjacency detection, reaction-diffusion equation

## I. INTRODUCTION

In many applications of mathematical modeling, continuum equations are used to describe the evolution of discrete biological systems such as tumors, epithelia, animal populations [1] etc. However, sometimes discrete effects may become important [2]. This is especially true when modeling the initial evolution of cancer, which is thought to originate within a single cell [3]. Within the class of agent-based (individual-based) models, cellular tissues are modeled as a set of strongly-interacting discrete objects. At present, it seems reasonable to consider the cell as the smallest entity in these models, though this is not stringent (compare e. g. the extended Potts model [4]). For agent-based models, the concept of the cellular automaton [5] has proven very useful, since it allows to describe cells by simple interaction rules. Tumor growth for example has successfully been modeled with cellular automata [6]. However, most of the current agent-based models are implemented on a lattice. In models where a single lattice site is occupied by a single cell, volume-nonconserving events such as proliferation require far-reaching configuration changes on the lattice, which comes along with rupture of intercellular bindings on a large scale [7]. This leads to the necessity of deriving effective interaction rules, which can often not be easily related to physical laws. This problem can be alleviated as well by allowing for shape fluctuations of cells, either on a lattice with the Potts [4] or the hyphasma [8] model or off-lattice with a boundary-based model [9, 10]. The approaches where the dynamics of the boundary is considered, use a dramatically increased number of dynamic variables and thereby the necessary calculation time increases. As an advantage however, physically-motivated interactions can be used to calculate the cellular dynamics. Off-lattice center-based models [11, 12] allow physical interactions to be included without the disadvantage of the large number of dynamic variables. Thus, they represent a compromise between speed of numerical calculation and model accuracy.

We have previously applied an off-lattice center-based model to multicellular tumor spheroids [13]. In comparison to continuum approaches [14] it turned out that agent-based models have greater potential to describe realistic biological systems. Keeping in mind that continuum models also arise from averaging (thereby deleting information), this is not a big surprise. However, it must be said that the degree of model complexity should always be limited by the experimental signature and for many experimental signatures continuum models will suffice.

In this article, we set up an off-lattice center-based model that is intrinsically consistent and is also based on physical interactions as far as possible. This has the advantage that the model can be falsified.

---

\*Electronic address: g.schaller@figss.uni-frankfurt.de

## II. THE EPIDERMIS

The epidermis is a stratified squamous epithelial tissue. It does not contain separate blood vessels and is therefore dependent on diffusion of nutrients from the dermis situated below. The epidermis can be divided into several layers [15]:

The innermost *stratum germinativum* or *stratum basale* (basal layer) is a monolayer, in which most cell divisions occur. It is separated from the dermis below by a basal membrane, which has a ruffled structure at fingers, palms and soles of feet. A fraction of the cells created there by cell division travels upwards into the *stratum spinosum*, where most cells are interconnected by desmosomes, which leads to a spiny cell appearance. Within this layer, the process of cornification begins: The cytoplasm loses water and is filled with keratin filaments. Within the *stratum granulosum*, cells die off and their shape flattens. This special pathway of cell death is also called anoikis. The *stratum lucidum* is a thin layer that is dominantly expressed at hand and feet and functions as a barrier against all possible intruders. Completely cornified cells mark the *stratum corneum*, which is clearly distinguishable from the layers below. This layer does not contain viable cells and constitutes an efficient barrier for water and many solutes. Note that the thickness of this layer varies strongly for different regions of the skin [15]. The upper part of this layer, where the cellular material detaches by dissolving intercellular contacts, is also called *stratum disjunctum*.

Within this article, only three layers will be distinguished: The term *stratum medium* will be used as a combination for all layers not belonging to the *stratum germinativum* or the *stratum corneum*.

The cell types encountered in the epidermis are keratinocytes, melanocytes, Langerhans cells, and Merkel cells. Of these, the dominant fraction is constituted by the keratinocytes with roughly 75000 cells per square mm [16, 17].

Keratinocytes are produced in the *stratum germinativum* by cell division. In order to maintain epidermal homeostasis, in average one of the two daughter cells must leave the basal layer and travel upwards. The keratinocyte remaining in the basal layer will be termed stemcell further-on. The cell traveling upwards transforms into a fully-differentiated keratinocyte – possibly undergoing transit amplifying proliferations [18] – and reaches the surface after about 12 to 14 days. During this passage, the keratinocytes also follow the process of cornification.

Melanocytes migrate to the dermis during embryonic development. These dendritic cells are distributed within the basal layer, and their density is relatively constant between individuals and races with approximately 2000 cells per square mm [15, 16, 19]. They adhere to the basal membrane via hemi-desmosomes. The purpose of melanocytes is to produce melanin and to provide it to keratinocytes and hair with their dendrites – the connected cells are also termed epidermal melanocyte unit [15]. Melanin protects the skin from the ionizing effects of electromagnetic radiation, and it is accumulated above the keratinocyte nuclei. Differences in skin color mainly result from different levels of melanin. Tumors arising from cancerous melanocytes are also called melanoma. Since most cancerous melanocytes still produce melanin, such tumors have a characteristic black color. If they are diagnosed and excised at an early stage, the prognosis is very good. The prognosis degrades rapidly for melanoma at later stages. Therefore, the early and secure diagnosis of this disease is a challenging problem.

Langerhans cells are dendritic cells of the immune system. There is evidence that they collect antigens via phagocytosis and present them after transforming to dendritic cells in lymph nodes.

Merkel cells are found close to some hair follicles in mammalian epidermis. Though there is no definite function in skin known, it is believed that these cells play a role in sensation.

Since neither effects of the immune system nor the mechanisms of sensation will be studied here, the latter two cell types will not be contained in the *in silico* representation and will not be discussed further.

The diffusional properties of the skin have important implications on medication applied to this tissue. With an observed strong increase of the manifestation of melanoma [19], studies of melanoma development are of huge importance. Within this article, some simple related questions will be addressed using an off-lattice agent-based approach.

## III. THE MODEL

In view of the complicated matter in reality, any model will inevitably simplify the system by neglecting properties that we consider to be less important. Starting from this perspective, the following approximation may seem reasonable:

Within the model, cells are represented as adhesively and elastically interacting, compressible spheres of time-dependent radii. Processes such as cell proliferation and cell death correspond to insertion or removal of spheres to the system. Similarly, cell growth enters the time-dependent cell radii. In analogy to the cell cycle, the model cells can assume different internal states. In addition, they consume nutrients and their presence changes the diffusive properties within the tissue.

The specificities and consequences of this paradigm will be examined in detail in the following sections.

### A. Intercellular Contact Model

Already the dynamics of rigid bodies in contact is a difficult problem, as the local geometry at the contact region will strongly influence the involved forces. Therefore, most contact models applied in practice are not motivated by microscopic assumptions but rather mimic the realistic behavior. In principle, for cellular interactions these contact models all have to fulfill two basic conditions

1. they exhibit strong repulsive forces for large deformations,
2. they have a bound state for small deformations.

These conditions are fulfilled by a large variety of contact models. For example, the general Lennard-Jones potential  $V(x) = Ax^{-\alpha} + Bx^{-\beta}$  between two objects placed at  $\mathbf{r}_i$  and  $\mathbf{r}_j$ , where  $x = |\mathbf{r}_i - \mathbf{r}_j|$ , has been successfully applied in physics to model the interactions of atoms [20]. Since  $A$ ,  $B$ ,  $\alpha$ , and  $\beta$  are model parameters, the potential can be fit to approximate the interaction of other systems such as e. g. grains [21] as well. Note that with a potential ansatz, viscous effects are not included.

A model describing viscous and also plasticity effects resulting from dissipative effects of both the extracellular matrix and the cytoskeleton can be constructed from a mechanical analog: Simple mechanical elements such as the dashpot and the spring are connected to a mechanical network. These networks then define a set of linear ordinary differential equations, which can be solved to obtain for example the cellular deformation as a function of time, see e. g. [22, 23]. These models however require a large set of parameters and facing the large uncertainty about inner-cellular elastic or dampening constants they must be used as fit models. A possible approach would be to derive the elastic and viscous parameters of such a mechanical network from a microscopic model of the cell. If one only considers the contribution of the cytoskeleton, a popular approach is the explanation of cellular properties by tensegrity structures (acronym derived from “tensional integrity”) [24, 25], which can be envisioned as a combination of rigid elements (usually bars) that are connected by elastic cables. Pressure and tension cooperate to stabilize the whole structure.

Within this article we have chosen a different approach, the Johnson-Kendall-Roberts (JKR) model [26, 27] – supplemented with viscous forces that are specified in subsection III C. The JKR-model includes elastic and adhesive (but non-viscous) interaction of solid spheres and it has been verified experimentally for soft materials such as rubber. In addition, it is often used in a biological context to estimate cellular parameters from experimental observations (JKR-test, [28]). Thus, one can at least on short time scales hope, that even though the parameters derived from such measurements [29] will not yield a correct description of the cytoskeleton (which is known to be viscoplastic), their usage in the model will at least lead to dynamics similar to that observed in the experiments.

The characteristics of the JKR contact model relevant for our considerations can be summarized as follows: Two spheres  $i$  and  $j$  placed at positions  $\mathbf{x}_i$  and  $\mathbf{x}_j$ , having radii  $R_{i/j}$ , Young moduli  $E_{i/j}$ , Poisson moduli  $\nu_{i/j}$ , and contact surface energy density  $\sigma_{ij}$  underlie the interaction force [27]

$$F_{ij}^{\text{JKR}} = \left[ \frac{K_{ij}a_{ij}^3}{R_{ij}} - \sqrt{6\pi\sigma_{ij}K_{ij}a_{ij}^3} \right], \quad (1)$$

where  $a_{ij}$  denotes the radius of the circular contact area between the deformed spheres,  $R_{ij}$  the reduced radius, and  $K_{ij}$  incorporates the combined elastic properties

$$R_{ij} = \frac{R_i R_j}{R_i + R_j}, \quad K_{ij} = \frac{1}{\frac{3}{4} \left( \frac{1-\nu_i^2}{E_i} + \frac{1-\nu_j^2}{E_j} \right)}. \quad (2)$$

For vanishing adhesive properties ( $\sigma_{ij} = 0$ ) one recovers the purely elastic Hertz model [30, 31]. The contact radius  $a_{ij}$  is related to the indentation (see figure 1 left panel)  $h_{ij} = R_i + R_j - |\mathbf{x}_i - \mathbf{x}_j|$  via [27, 32]

$$h_{ij} = \frac{a_{ij}^2}{R_{ij}} - \sqrt{\frac{8\pi\sigma_{ij}}{3K_{ij}}} \sqrt{a_{ij}}, \quad (3)$$

which may have – depending on the value of  $h_{ij}$  – none, one, or two solutions with  $a_{ij} > 0$ . For relatively small adhesion  $\sigma_{ij}/(K_{ij}R_{ij}) \ll 1$ , the second term on the right hand side can be neglected, and the solution  $a_{ij} \approx \sqrt{h_{ij}R_{ij}}$  can be inserted into equation (1) to yield an approximate force-distance relationship [32]

$$F_{ij}^{\text{JKR}} \approx \left[ K_{ij}R_{ij}^2 \left( \frac{h_{ij}}{R_{ij}} \right)^{3/2} - \sqrt{6\pi\sigma_{ij}K_{ij}R_{ij}^3} \left( \frac{h_{ij}}{R_{ij}} \right)^{3/4} \right], \quad (4)$$

which will be referred to as JKR force further-on throughout this article. The force is negative (adhesive) for small overlaps  $h_{ij} = (R_i + R_j - d_{ij}) \Theta(R_i + R_j - d_{ij})$  – where  $d_{ij}$  denotes the distance between the sphere centers – and becomes positive (repulsive) for larger overlaps. Note that – independent on the approximation of small adhesion in (3) – the adhesive force has the maximum magnitude

$$F_{ij}^{\text{adh}} = -\frac{3}{2}\pi\sigma_{ij}R_{ij}, \quad (5)$$

which is also independent on the elastic cell properties and thus allows an estimate of  $\sigma_{ij}$  from cell-doublet-rupture experiments such as e. g. [33, 34]. Since in reality the spheres underlie deformation, the resulting approximate sphere contact surface in JKR theory

$$A_{ij}^{\text{JKR}} = \pi a_{ij}^2 \approx \pi h_{ij} R_{ij} \quad (6)$$

is in general different from the virtual contact surface that would follow intuitively from the sphere overlap region (figure 1 left panel). The above contact surface has been chosen in the model to make it intrinsically consistent. In the following, the short hand notations  $R_{\min} = \min\{R_i, R_j\}$  and  $R_{\max} = \max\{R_i, R_j\}$  will be used with suppressed indices.

For the approximate theory (4) one can introduce a two-body interaction potential via

$$F_{ij}^{\text{JKR}} = -\frac{\partial V^{\text{JKR}}}{\partial d_{ij}} = +\frac{\partial V^{\text{JKR}}}{\partial h_{ij}} = \frac{1}{R_{ij}} \frac{\partial V^{\text{JKR}}}{\partial h_{ij}/R_{ij}}, \quad (7)$$

which leads for our case to

$$V_{ij}^{\text{JKR}}(h_{ij}/R_{ij}) = \frac{2}{5}K_{ij}R_{ij}^3 \left(\frac{h_{ij}}{R_{ij}}\right)^{5/2} - \frac{4}{7}\sqrt{6\pi\sigma_{ij}K_{ij}R_{ij}^5} \left(\frac{h_{ij}}{R_{ij}}\right)^{7/4}, \quad (8)$$

which is a special case of the Lennard-Jones potential (compare figure 1). However, here the parameters have either been linked to cellular properties that are accessible by independent experiments or been fixed by microscopic assumptions.

The quantity  $h_{ij}/R_{ij}$  describes the relative position of both spheres and is related to the orthogonal sphere distance (compare [35])

$$\pi(\hat{\mathbf{x}}, \hat{\mathbf{y}}) = (\mathbf{x} - \mathbf{y})^2 - R_x^2 - R_y^2 \quad (9)$$

for the spheres  $\hat{\mathbf{x}} = (\mathbf{x}, R_x^2)$  and  $\hat{\mathbf{y}} = (\mathbf{y}, R_y^2)$  via

$$\pi(\hat{\mathbf{r}}_i, \hat{\mathbf{r}}_j) = \left(\frac{h_{ij}}{R_{ij}}\right)^2 R_{ij}^2 - 2\left(\frac{h_{ij}}{R_{ij}} - 1\right) R_i R_j, \quad (10)$$

compare also figure 2 left panel.

The full JKR-theory has several shortcomings:

1. It is only valid for small deformations  $h_{ij}/R_{ij} \ll 1$ , since the linear elastic theory assumed in the derivation of (1) is not valid for large deformations [31]. In addition, it approximates the cytoskeleton as a homogeneous solid, which is not the case [28]. Regarding the numerical solution of the interacting particle system, this has the consequence that some cells may be completely covered by others, since the JKR force (4) does not diverge at complete overlaps. To circumvent this, a modified interaction potential has been used, which displays this divergence

$$\begin{aligned} V(x) &= f(x)V^{\text{JKR}}(x), \\ f(x) &= \begin{cases} \frac{(x_d - x_m)^2}{(x_d - 2x_m)(x_d - x)} - \frac{x}{x_d - 2x_m} & : x_m \leq x \leq x_d \\ 1 & : \text{else} \end{cases}, \end{aligned} \quad (11)$$

if one chooses as matching point  $x_m = 1$  and as point for divergence  $x_d = 2 + 2R_{\min}/R_{\max}$  (compare figure 2). The choice of this modified potential only led to significantly different growth dynamics for  $\mathcal{O}(10^4)$  cells if cellular growth was constrained by static boundaries [36], which indicates that the used drag forces (see section III C) were small enough to enable fast relaxation.

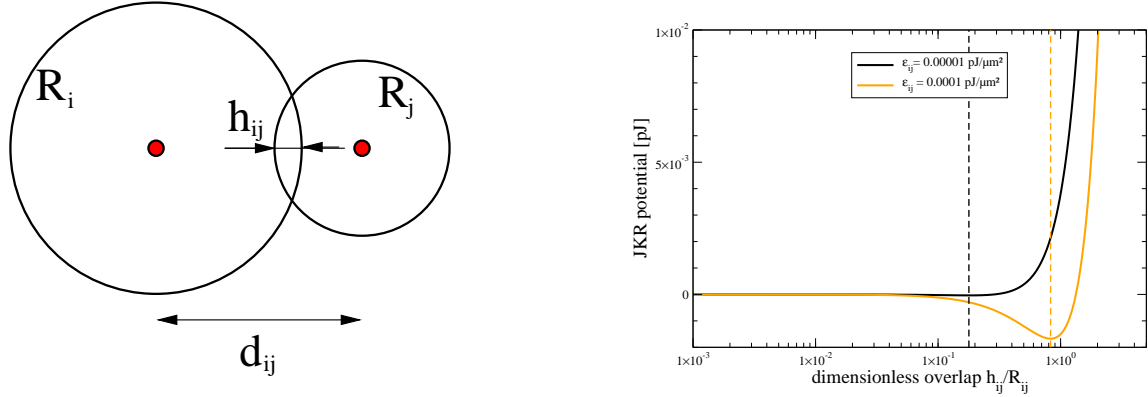


FIG. 1: Illustration of the interaction model. The dynamics of two elastic and adhesive spheres in contact can be described with the JKR-potential. **Left:** The virtual sphere overlap  $h_{ij}$  can be calculated from the sphere distance  $d_{ij} = |\mathbf{x}_i - \mathbf{x}_j|$  and equilibrium radii  $R_i$  and  $R_j$ . In real-world scenarios, the spheres would evidently deform thus giving rise to a deformed contact radius  $a_{ij}$  (not shown). **Right:** The existence of adhesive forces gives rise to bound states (right, minima at dashed lines). Their position and depth strongly depends on the parameters  $\sigma_{ij}$  and  $K_{ij}$ . Note that the potential does not diverge at  $h_{ij}/R_{ij} = 2 + 2R_{\min}/R_{\max}$  (complete overlap). The curves on the right have been computed using the following (physiological) values  $K_{ij} = 1000$  Pa,  $R_{ij} = 2.5$   $\mu\text{m}$ .

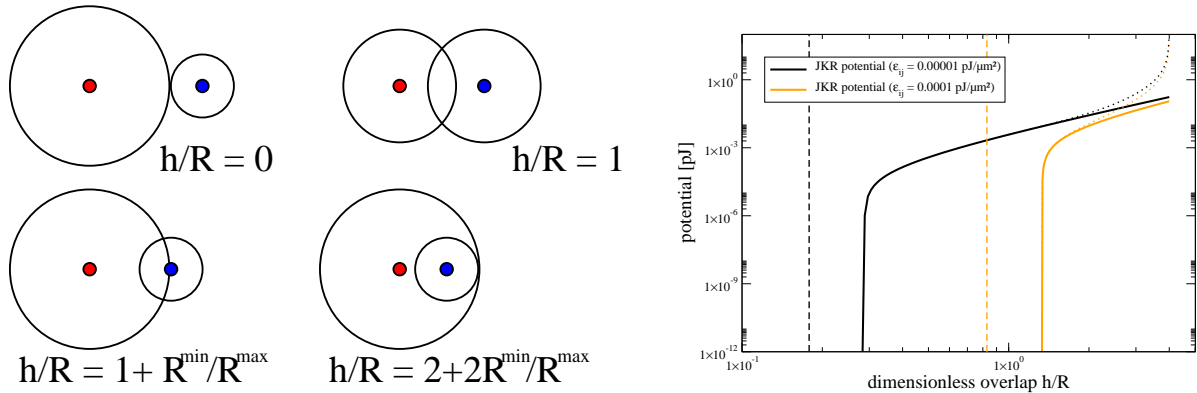


FIG. 2: Sphere overlaps and modification of the interaction potential. **Left:** Typical contact configurations corresponding to special values of the dimensionless sphere distance  $h_{ij}/R_{ij}$  – for clarity the indices have been dropped. For vanishing virtual overlap, one obtains  $h/R = 0$ , whereas for the case when the center of the smaller sphere is placed exactly on the boundary of the larger one, one has  $h/R = 1 + R_{\min}/R_{\max}$ . Complete inclusion of the smaller sphere within the larger one corresponds to even larger values of  $h/R$ . In this regime, JKR theory is not valid anymore. **Right:** For this reason, the JKR interaction has been supplemented with a pole at complete sphere overlap. Matching has been performed at  $h_{ij}/R_{ij} = 1$ , where one has  $\pi(\hat{\mathbf{r}}_i, \hat{\mathbf{r}}_j) = R_{ij}^2$ . In the physiological regime, the potential is unchanged. Parameters have been chosen as in figure 1.

2. The JKR-theory does neither include viscous effects arising from the cytoskeleton nor dissipation occurring in the extracellular matrix. Therefore, the model will be supplemented with additional drag forces, which are specified in subsection III C.
3. The original result (1) has been derived as a pure two-body interaction [27], which is also the case for its purely elastic precursor [30, 31]. However, for many adhering spheres already for small individual deformations additional forces will come into play, since
  - the spheres are pre-stressed,
  - the circular contact regions of various cells may overlap.

Thus, the JKR model does not correctly describe cellular compression for multiple overlaps. The extent of

this shortcoming will critically depend on the current adjacency topology which makes an analytical approach infeasible. For numerical ease and due to missing estimates in this article the following practitioners approach has been chosen. Below the target cell volume  $V_{i/j}^{\text{target}}$  the cell experiences additional repulsive – isotropic – forces due to compression of the cytoskeleton. Then, the resulting additional repulsive force acts in the direction of the neighbors  $j$  with magnitude

$$F_{ij}^{\text{comp}} = A_{ij} \left[ \frac{E_i}{3(1-2\nu_i)} \left( 1 - \frac{V_i}{V_i^{\text{target}}} \right) + \frac{E_j}{3(1-2\nu_j)} \left( 1 - \frac{V_j}{V_j^{\text{target}}} \right) \right], \quad (12)$$

where  $V_{i/j}$  denote the current cellular sphere volumes (reduced by the overlaps with neighboring spheres) and  $A_{ij}$  the circular JKR contact surfaces in equation (6). Note that owing to model simplicity, neither volume nor surface corrections [13] are calculated with the Voronoi tessellation in this article.

4. Whereas the forces in the approximate model (4) only depend on the actual relative cellular positions, a more realistic scenario would have to include hysteresis effects, as adhesive intercellular bonds form after contact [34]. This however would require to keep track of the time evolution of cellular adjacencies. In part, the time evolution can be incorporated into the time dependence of the adhesive parameters

$$\sigma_{ij} = \frac{\sigma^{\max}}{2} \left[ C_i^{\text{rec}}(t) C_j^{\text{lig}}(t) + C_i^{\text{lig}}(t) C_j^{\text{rec}}(t) \right], \quad (13)$$

where the  $0 \leq C_{i/j}^{\text{rec/lig}}(t) \leq 1$  represent the receptor or ligand densities on the cell membrane – normalized relative to a maximum density, and  $\sigma^{\max}$  is the maximum adhesion energy, respectively. It must be noted that also the cytoskeleton reorganizes and thereby the intrinsic cell shape will not remain spherical after contact. A full description of these effects would therefore not only require time-dependent elastic parameters ( $E_i, \nu_i$ ), but also the implementation of a dynamically changing intrinsic equilibrium cell-shape, which is presumably not within the reach of a center-based model [37].

5. In addition, the derivation of the JKR model relies on the fact that only normal forces act. For cell doublets with friction, shear forces will in reality exist. It is assumed here that the net effect of shear forces on the validity of the JKR approach can be neglected, such that they can be independently included in the drag forces.

At least for keratinocytes the application of the JKR model to cell doublet rupture experiments [34] leads to discrepancies between the visual equilibrium distance and the equilibrium distance predicted by the full JKR-model (1): If one derives via equation (5) the maximum adhesion energy density from the maximum rupture force recorded in [34], the resulting equilibrium distance predicted by (1) is considerably different than observed in the figures of the same publication: The indentation  $h_{ij}$  resulting from equation (3) becomes negative (pointing to extrapolation of JKR theory beyond the region of its validity), whereas for the approximate JKR model, the limiting condition  $\sigma_{ij}/(K_{ij}R_{ij}) \ll 1$  is certainly violated, which would lead to considerably smaller equilibrium distances (larger indentations) than in reality. For example, for cell-cell contact times smaller than 30 seconds, average rupture forces of 20 nN have been measured [34]. Assuming  $K_{ij} = 1000$  Pa and  $R_{ij} = 2.5 \mu\text{m}$  one would thereby find from equation (5) an adhesion energy density of  $\sigma^{\max} \approx 0.0017 \mu\text{N}/\mu\text{m}$ . However, then the equilibrium distances resulting from equations (1) or (4), respectively, are inconsistent with the equilibrium distances in [34]. This indicates that the JKR model is not directly applicable to strongly adhesive cells. For larger times, the discrepancy becomes even worse.

However, we expect that all these shortcomings are not major sources of error if one aims at analyzing control mechanisms. An improved contact model could generally be included in such simulations, but it should be reasonably motivated by microscopic theories or experimental data first.

## B. Random Forces

Due to thermal fluctuations, any particle in a solution will be subject to random forces (Brownian motion). In addition, some cell types exhibit intrinsic (active) movement which sometimes appear to be of random nature and thus follow the same mathematics as Brownian motion. For systems with these characteristics, the time-dependent stochastic forces  $\mathbf{F}(t)$  modeling the random behavior have to fulfill two conditions [38]:

1. their mean vanishes  $\langle \mathbf{F}(t) \rangle = 0$  and
2. the forces are not correlated, i. e.,  $\langle \mathbf{F}(t_1) \cdot \mathbf{F}(t_2) \rangle = 3\xi^2 \delta(t_1 - t_2)$ .

The parameter  $\xi$  thereby quantifies the strength of the stochastic fluctuations. The movement of single cells in a solution is highly overdamped [12], and any stochastic force fulfilling the above conditions will lead in the Langevin equation to a diffusion-like evolution of cellular distribution, i. e., in the absence of additional forces the squared displacement will be given by

$$\langle \mathbf{r}^2(t) - \mathbf{r}_0^2 \rangle = 3 \frac{\xi^2}{\gamma^2} t = 6Dt, \quad (14)$$

where  $D$  is the corresponding (observed) diffusion coefficient and  $\gamma$  is a dampening constant, which effectively describes the strength of friction. The above identity is also known as the fluctuation dissipation theorem, since it connects the fluctuations ( $\xi$ ) with the dissipation ( $\gamma$ ). If this dynamics is observed for free spherical cells in medium, the friction constant can for highly-damped dynamics be well approximated by the Stokes friction  $\gamma_0 = 6\pi\eta R$ , where  $R$  represents the radius of the cell and  $\eta$  the viscosity of the surrounding medium. Evidently, with the same random forces applied, cellular movement will be much smaller if drag forces due to cellular bindings are at work. For numerical implementations, a stochastic force fulfilling the above conditions can be given by [38]

$$F_i(t) = \frac{\xi}{\sqrt{\Delta t}} \chi_{0,1}^{\text{GAUSS}}, \quad (15)$$

where  $\Delta t$  describes the width of the timestep, and  $\chi_{0,1}^{\text{GAUSS}}$  is a random number drawn from a Gaussian distribution [39] with mean  $\mu_\chi = 0$  and width  $\sigma_\chi = 1$ .

It should be noted however, that active random eucaryotic movement in reality usually occurs with pseudopods [40]: The cell attaches protrusions to neighboring cells (or the extracellular matrix) and randomly pulls towards them. This has two further implications

- the stochastic forces become two-body forces, i. e., the neighbor cell that the pseudopod is attached to, is subject to the corresponding negative force [38]. Also, the forces act into the direction of the normals [41].
- Since the pseudopods do not enable pushing, the average stochastic force component into the direction of a given neighbor cell will not in general vanish. For example, at interfaces of dense tissue (where the pseudopods find resistance) and fluid (where no net force can be generated) one cannot expect the different contributions to compensate.

Since the intrinsic logic behind active cellular movement following Brownian mathematics is not fully understood and also active movement with pseudopods is not quantified for the cell types considered in the simulation (keratinocytes and melanocytes), we have chosen to implement stochastic forces via equation (15) as acting randomly on every cell that react passively to these in return.

### C. Equations of Motion

For  $N$  cells with positions  $\mathbf{x}_i(t)$  and radii  $R_i$  subject to cell-cell as well as cell-medium and cell-substrate interactions, the equations of motion can in the reference frame of motionless medium and boundaries be summarized as (compare also [22])

$$m_i \ddot{x}_i^\alpha = F_i^\alpha + \sum_{j \in \mathcal{NN}(i)} F_{ij}^\alpha - \sum_\beta \left( \gamma_i^{\alpha\beta} + \sum_{J \in \mathcal{NB}(i)} \Gamma_{iJ}^{\alpha\beta} \right) \dot{x}_i^\beta - \sum_{j \in \mathcal{NN}(i)} \sum_\beta \gamma_{ij}^{\alpha\beta} \left( \dot{x}_i^\beta - \dot{x}_j^\beta \right), \quad (16)$$

where  $\alpha, \beta \in \{0, 1, 2\}$  denote the Cartesian indices and  $i, j \in \{0, 1, \dots, N-1\}$  the cellular indices. The terming  $\mathcal{NN}(i)$  denotes all cells having direct contact with cell  $i$ . A set of neighboring cells containing as a subset the cells having direct contact is for efficiency reasons provided by the weighted Delaunay triangulation module we had developed and applied previously in [13, 42]. In contrast,  $\mathcal{NB}(i)$  denotes the boundaries in contact with cell  $i$ . Since for most problems few boundary conditions will be given, these are hard-wired in the code for every specific problem individually. Note also that the back-reaction of the cells on the boundaries is neglected implicitly assuming that the boundaries are stationary.

The first term on the right-hand side  $F_i^\alpha$  may generally include deterministic (for example, crawling forces on a substrate) and stochastic (e. g. Brownian motion) forces on a single cell, whereas the second term  $\sum_{j \in \mathcal{NN}(i)} F_{ij}^\alpha$  includes the intercellular two-body forces (e. g. stochastic two-body forces or the deterministic JKR-force, compare

subsections III A and III B). The third term  $\left( \sum_{\beta} \gamma_i^{\alpha\beta} + \sum_{\beta} \sum_{J \in \mathcal{NB}(i)} \Gamma_{iJ}^{\alpha\beta} \right) \dot{x}_i^{\beta}$  incorporates cell-medium as well as cell-boundary friction, whereas the last term in equation (16) includes cell-cell friction.

Note that equation (16) should generally be completed by an equation describing the evolution of torque as in [21], where the kinetics of grains had been modeled. However, with the strong cellular bindings existent in tissue, torque could only lead to macroscopically spinning tissues, which is not observed in the epidermis, since it is attached to the rigid basal membrane. The insertion of torque into the model is thus possible, but has been only included effectively here by energy dissipation via drag forces. A usual choice for cell-medium friction is the well-known Stokes-relation  $\gamma_i^{\alpha\beta} = 6\pi\eta R_i \delta^{\alpha\beta}$  [43] already introduced in subsection III B. The friction coefficients and two-body forces fulfill the following conditions:

$$\begin{aligned} \gamma_{ij}^{\alpha\beta} &= \gamma_{ji}^{\alpha\beta}, & F_{ij}^{\alpha} &= -F_{ji}^{\alpha} & (\text{Newton's third axiom}), \\ \gamma_{ij}^{\alpha\beta} &= \gamma_{ij}^{\beta\alpha} & & & (\text{projection operator property}), \\ \gamma_i^{\alpha\beta} &= \gamma_i \delta^{\beta\alpha} & & & (\text{isotropy}), \\ \gamma_{ii}^{\alpha\beta} &= 0 & & & (\text{no self-friction}). \end{aligned} \quad (17)$$

Note that in a strict sense, Newton's third axiom only applies to the total two-body force. However, here the model should consistently include contact forces  $F_{ij}^{\alpha}$  and drag forces  $\gamma_{ij}^{\alpha\beta} (\dot{x}_i^{\beta} - \dot{x}_j^{\beta})$ , which may act independently from each other. Therefore, *actio et reactio* has been assumed to act separately. The symmetry in  $(\alpha, \beta)$  of the friction coefficients also arises from the symmetry properties of the projection operators: The drag forces expressed by the friction coefficients may be divided in normal drag forces and tangential (shear) drag forces. Assuming that they are proportional to the effective contact area between two cells  $i$  and  $j$

$$A_{ij}^{\text{eff}} = A_{ij} \frac{1}{2} \left[ C_i^{\text{rec}}(t) C_j^{\text{lig}}(t) + C_i^{\text{lig}}(t) C_j^{\text{rec}}(t) \right] \quad (18)$$

and to the normal or tangential projection of the velocity differences, respectively, the friction coefficients take the form

$$\begin{aligned} \gamma_{ij}^{\alpha\beta} &= A_{ij}^{\text{eff}} \left( \gamma_{\parallel} \mathcal{P}_{ij,\parallel}^{\alpha\beta} + \gamma_{\perp} \mathcal{P}_{ij,\perp}^{\alpha\beta} \right) (1 - \delta_{ij}), \\ \Gamma_{iJ}^{\alpha\beta} &= A_{iJ} \left( \gamma_{\parallel} \mathcal{P}_{iJ,\parallel}^{\alpha\beta} + \gamma_{\perp} \mathcal{P}_{iJ,\perp}^{\alpha\beta} \right). \end{aligned} \quad (19)$$

The friction constant  $\gamma_{\perp}$  predominantly describes internal friction within the cytoskeleton [41], since force contributions for movements normal to the cell-cell contact surface are already contained within the JKR interaction model. The friction constant  $\gamma_{\parallel}$  is set to vanish within this article thereby implicitly assuming that dampening due to friction within the cytoskeleton is much smaller than dampening due to cell-cell bindings. In contrast, the tangential friction constant  $\gamma_{\parallel}$  describes drag forces resulting from broken bindings during movements tangential to the intercellular contact plane [12, 41]. For model consistency, the used contact surfaces are chosen identical with the JKR contact surface (6). Since over a wide range of physiological overlaps this relates to the spherical overlap that would result from undeformed spheres by about a factor of two, a different choice of the contact surface could be compensated by appropriately changed friction parameters.

The intercellular tangential and perpendicular projectors are given by

$$\mathcal{P}_{ij,\parallel}^{\alpha\beta} = \delta^{\alpha\beta} - n_{ij}^{\alpha} n_{ij}^{\beta}, \quad \mathcal{P}_{ij,\perp}^{\alpha\beta} = n_{ij}^{\alpha} n_{ij}^{\beta}, \quad (20)$$

and the cell-boundary projectors

$$\mathcal{P}_{iJ,\parallel}^{\alpha\beta} = \delta^{\alpha\beta} - n_{iJ}^{\alpha} n_{iJ}^{\beta}, \quad \mathcal{P}_{iJ,\perp}^{\alpha\beta} = n_{iJ}^{\alpha} n_{iJ}^{\beta}, \quad (21)$$

respectively. In the above projection operators,  $\mathbf{n}_{ij}$  represents the normal vector pointing from cell  $i$  towards cell  $j$  (compare also figure 3 left panel), whereas  $\mathbf{n}_{iJ}$  denotes the normal vector of the boundary  $J$  at the contact point with cell  $i$ . Note that with these projection operators, the conditions on the friction coefficients (17) are automatically fulfilled.

In the over-damped approximation  $m_i \ddot{x}_i^{\alpha} \approx 0$ , equation (16) can be cast into the following form,

$$\sum_{k,\beta} \left\{ \left[ \gamma_k^{\alpha\beta} + \sum_j \gamma_{kj}^{\alpha\beta} + \sum_J \Gamma_{kJ}^{\alpha\beta} \right] \delta_{ik} - \gamma_{ik}^{\alpha\beta} \right\} \dot{x}_k^{\beta} = F_i^{\alpha} + \sum_j F_{ij}^{\alpha}. \quad (22)$$

From the properties of the friction coefficients it is evident that the linear system is symmetric and also diagonally dominant as long as  $\gamma_i^{\alpha\alpha} + \sum_J \Gamma_{iJ}^{\alpha\alpha} > 0 \quad \forall i, \alpha$ , which holds true if  $\eta$  does not vanish, as all diagonal entries in the projection operators (20) and (21) are positive. In addition, it must be noted that the system will be extremely sparsely populated as the friction coefficients vanish for all cells not being in direct contact, see subsection III D for an example.

#### D. Numerical solution

An example including cell-cell and cell-boundary friction is illustrated in figure 3. Indeed, for this special example all non-isotropic friction coefficients vanish except  $\gamma_{03}^{\alpha\beta}, \gamma_{04}^{\alpha\beta}, \gamma_{23}^{\alpha\beta}, \gamma_{34}^{\alpha\beta}, \Gamma_0^{\alpha\beta}, \Gamma_4^{\alpha\beta}$ . Consequently, for this example the

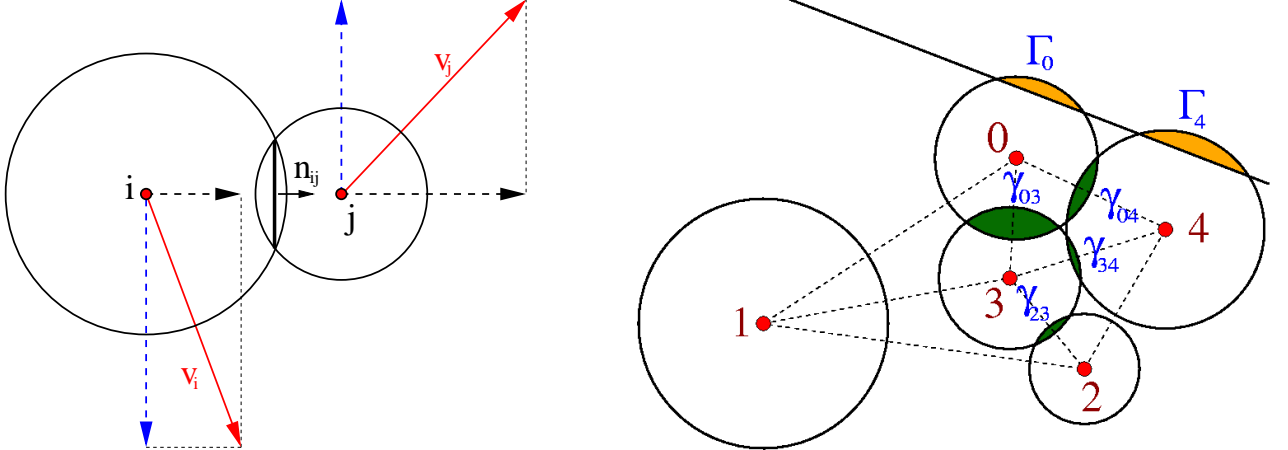


FIG. 3: Two-dimensional illustration of intercellular force calculation. **Left:** The differential velocities between two cells  $i$  and  $j$  (circles) in contact may give rise to different drag forces, one proportional to the tangential part of the velocity difference and one proportional to the perpendicular part as indicated with dashed lines. **Right:** The dotted lines denote the weighted Delaunay triangulation of the set of spheres. Only spheres with cell-cell contact (overlap, dark grey) will contribute to intercellular friction and to intercellular forces. Cell-boundary contact (overlap, light grey) will contribute to cell-medium friction and to cell-boundary forces. Spheres that are not connected in the weighted Delaunay triangulation will not contribute.

system (22) would assume the form

$$\begin{pmatrix} \Gamma_0 + \gamma_0 + \gamma_{03} + \gamma_{04} & \mathbb{O} & \mathbb{O} & -\gamma_{03} & -\gamma_{04} \\ \mathbb{O} & \gamma_1 & \mathbb{O} & \mathbb{O} & \mathbb{O} \\ \mathbb{O} & \mathbb{O} & \gamma_2 + \gamma_{23} & -\gamma_{23} & \mathbb{O} \\ -\gamma_{03} & \mathbb{O} & -\gamma_{23} & \gamma_3 + \gamma_{03} + \gamma_{34} & -\gamma_{34} \\ -\gamma_{04} & \mathbb{O} & \mathbb{O} & -\gamma_{34} & \Gamma_4 + \gamma_4 + \gamma_{04} + \gamma_{34} \end{pmatrix} \begin{pmatrix} \dot{x}_0 \\ \dot{x}_1 \\ \dot{x}_2 \\ \dot{x}_3 \\ \dot{x}_4 \end{pmatrix} = \begin{pmatrix} \mathbf{F}_0 + \mathbf{F}_{03} + \mathbf{F}_{04} + \mathbf{F}_{0B} \\ \mathbf{F}_1 \\ \mathbf{F}_2 + \mathbf{F}_{23} \\ \mathbf{F}_3 + \mathbf{F}_{30} + \mathbf{F}_{32} + \mathbf{F}_{34} \\ \mathbf{F}_4 + \mathbf{F}_{40} + \mathbf{F}_{42} + \mathbf{F}_{43} + \mathbf{F}_{4B} \end{pmatrix}, \quad (23)$$

where in three dimensions the symbols  $\mathbf{F}_i$  and  $\mathbf{x}_i$  denote vectors in  $\mathbb{R}^3$  and  $\mathbb{O}$ ,  $\gamma_{ij}$ ,  $\gamma_i$ , and  $\Gamma_i$  denote  $3 \times 3$  matrices. This system is evidently symmetric, sparsely populated and weakly diagonally dominated, since  $\gamma_i^{\alpha\alpha} + \Gamma_i^{\alpha\beta} > 0 \quad \forall i, \alpha$ . In addition, all friction coefficients are positive. One can show, that this suffices to guarantee positive definiteness of the dampening matrix. Note that the number of next neighbors in contact corresponds to the number of off-diagonal blocks in the dampening matrix, such that the system becomes extremely sparse for large matrices.

Such systems can for efficiency be supplemented with the weighted Delaunay triangulation of a set of spheres for adjacency detection [42]. Since the dampening matrix is positive definite, the method of conjugate gradients [44] is well suited to the problem. However, since realistic systems will contain much more than 5 cells, the matrices would not fit into main memory, if stored completely. Fortunately, the matrices are only sparsely populated and the

method of conjugate gradients can efficiently be combined with a row-indexed sparse storage scheme [45] to compute a solution  $\dot{x}_i^\alpha$ . Note that the solution of the full system is an improvement over existing models [12], where the tangential projector  $\mathcal{P}_{ij}^{\alpha\beta}$  had for simplicity been approximated with the identity operator.

The reaction-diffusion equation for the molecules

$$\frac{\partial u}{\partial t} = \nabla [D(\mathbf{r}; t) \nabla u] + Q(\mathbf{r}; t) \quad (24)$$

has been solved in three dimensions using the Crank-Nicolson scheme [46] with a discrete element method on a cubic lattice using the algorithm of biconjugate gradients [45]. Note that due to the strongly varying diffusion coefficients in cornified and non-cornified tissue (see table I), the steady-state approximation is not applicable. The lattice constants have been chosen larger than the cellular diameters to ensure for validity of the discretization approximation [13]. Note that the reaction diffusion equation for the nutrients is made positive definite by cells entering necrosis below critical nutrient concentrations – necrotic cells do not consume nutrients, compare the next subsection. While the timestep of the simulation is determined by a maximum spatial cellular stepsize (fixed at  $0.5 \mu\text{m}$ ), the timestep of the reaction-diffusion grids has been divided into several substeps such that the Courant factor [45] is smaller than 1 in order to increase numerical accuracy. To connect the discrete reaction-diffusion grid with the spatially-continuous cellular positions, tri-linear interpolation has been used. In addition, the concentration has been fixed to vanish at grid nodes whose elementary cell did not contain cells. At grid nodes in the vicinity of cells the diffusive properties have been smoothly adapted in the range of the values given in table I.

### E. The cell cycle

Without representations of internal cellular states, the model would merely calculate the mechanical interaction between a number of adhesively and elastically interacting deformable spheres. Extending a previous agent-based modeling approach to the necessities of the epidermis, we distinguish between the following internal states in the model: M-phase, G<sub>1</sub>-phase, S/G<sub>2</sub>-phase, G<sub>0</sub>-phase, necrotic, cornified. The first four states are illustrated in figure 4 left panel. During G<sub>1</sub>-phase, the cell volume grows at a constant rate  $r_V$ , i. e., the radius increases according to

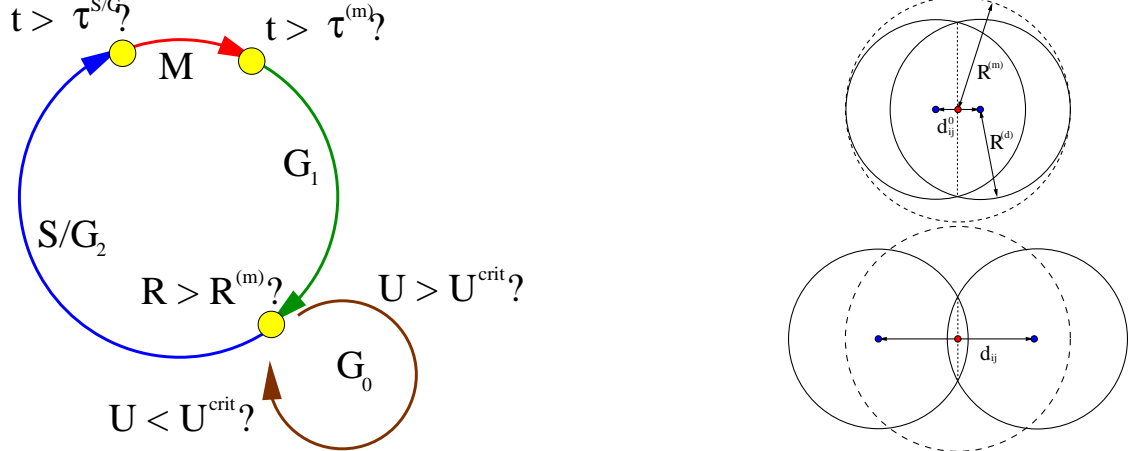


FIG. 4: **Left:** Model realization of the cell cycle. During cell division, cells reside in the M-phase for  $\tau^{(m)}$ . Afterwards, the cell volume increases at a constant rate in the G<sub>1</sub>-phase, until the pre-mitotic radius  $R^{(m)}$  has been reached. At the end of the G<sub>1</sub>-phase, the cell can either directly continue with the cell cycle or it can prolong the cycle time by entering the G<sub>0</sub>-phase, if the local concentration of the regulatory substance (water) exceeds a threshold  $U^{crit}$ . The G<sub>0</sub>-phase is left after an individual time drawn from a Gaussian distribution or if the local concentration of the regulating signal falls below the critical threshold. Depending on the local nutrient concentration, cells can enter necrosis at any time in the cell cycle (not shown). In addition, keratinocytes enter anoikis in the fourth cell generation after completion of the S/G<sub>2</sub>-phase. **Top right:** Displayed is the configuration right at cell division at the beginning of the M-phase. The radii of the daughter cells (solid circles) are reduced to ensure conservation of the target volume. **Bottom right:** At the end of the M-phase, the daughter cells have relaxed. Due to interaction with neighboring cells (not shown), the direction of mitosis may generally change during M-phase. An adaptive timestep ensures that contact is maintained.

$\dot{R} = (4\pi R^2)^{-1} r_V$ , until the cell reaches its final mitotic radius  $R^{(m)}$ . The volume growth rate  $r_V$  is deduced from the

minimum observed cycle time  $\tau^{\min}$  and the durations of the S/G<sub>2</sub>-phase and the M-phase. Afterwards, no further cell growth is performed. At the end of the G<sub>1</sub>-phase, a checkpointing mechanism is performed.

At this checkpoint, the cell can either enter the G<sub>0</sub>-phase or the S/G<sub>2</sub>-phase: A diffusible substance that moderates the cellular proliferation has been postulated in [47]. It is well known that the *stratum corneum* constitutes an effective barrier against the loss of water, its solutes, and other substances as well [18, 48, 49]. As the simplest model assumption, we will here assume the distribution of extracellular water to influence cell proliferation: If the local water concentration is below a critical value (model parameter), the cell will directly continue the cell cycle, whereas in the other case the cell cycle will be prolonged by the cell switching into the G<sub>0</sub>-phase. Note that the assumption of a different moderating diffusible signal would not significantly change the model as long as it is not created or consumed by the cells in the epidermis themselves. Cells leave the G<sub>0</sub>-phase to enter the S/G<sub>2</sub>-phase if either the local water concentration falls below the threshold or after a maximum time has passed. This maximum time is drawn from a Gaussian-distributed random number generator. Note that within this article the S-phase and G<sub>2</sub>-phase are not distinguished, their inclusion would be a mere technical aspect. At the beginning of the phase the individual phase duration is determined using a normally-distributed random number generator [39] with a given mean and width. After this individual time has passed, the cells deterministically enter mitosis. Keratinocytes underly an exception at this point: After the fourth cell generation, this cell line cornifies (enters anoikis) [7, 18, 47]. Note that within this model, the difference between the S/G<sub>2</sub>-phase and the G<sub>0</sub>-phase is that the duration of the first is determined by the normally distributed individual time that can be derived from experiments, whereas the duration of the latter is also controlled by the temporal evolution of the local water concentration.

One should be aware that our classification of internal cellular states may not directly correspond to the realistic biological system. However, the only net effect of the existence of the G<sub>0</sub>-phase is the prolongation of the cell cycle time: Cells in G<sub>0</sub>-phase can serve as a reservoir of cells ready to start proliferating as soon as the local water concentration falls below a critical threshold. A different terminology or a placement of the G<sub>0</sub>-phase after or within the S/G<sub>2</sub>-phase would therefore not significantly change the model.

At the beginning of the mitotic phase – which lasts for about half an hour for most cell types – a mother cell divides and is replaced by two daughter cells. The radii of the daughter cells are decreased  $R^{(d)} = R^{(m)}2^{-1/3}$  to ensure conservation of the target volume during M-phase. In addition, they are placed at distance  $d_{ij}^0 = 2R^{(m)}(1 - 2^{-1/3})$  to ensure that in this first step the daughter cells do not leave the region occupied by the mother cell, see figure 4 right panels. The initial direction of mitosis is chosen randomly. However, when considering the cell types, keratinocyte stemcells divide asymmetrically, since by model assumption the upper daughter cell differentiates to a keratinocyte. After insertion of the new cell and resetting of the mother cell parameters, the new cells are left to their initially dominating repulsive forces (4). Note that an adaptive timestep derived from a maximum spatial stepsize ensures that the mitotic partners do not loose contact. As in the S/G<sub>2</sub>-phase the individual duration of the M-phase is determined using a normally-distributed random number generator. Afterwards, the daughter cells enter the G<sub>1</sub>-phase thus closing the cell cycle.

Viable cells can enter necrosis at any time as soon as the nutrient concentration at the cellular position falls below a cell-type specific critical threshold. As the dominant pathway to cell death, keratinocytes in contrast enter anoikis after completing S/G<sub>2</sub>-phase in the fourth generation. Naturally, necrotic or cornified cells do not consume any nutrients. In view of the unknown details of the cell loss process, we have assumed an exponential decay of receptor and ligand molecules on the cell membrane with a given rate  $\alpha$ , i. e.,

$$\dot{C}_i^{\text{rec/lig}} = -\alpha C_i^{\text{rec/lig}}. \quad (25)$$

In order to minimize the perturbation of the equilibrium distance following from equation (4), we have chosen to decrease the elastic modulus as well. To maintain for similar cells a constant equilibrium distance, this implies a decreasing elastic modulus according to

$$\dot{E}_i = -2\alpha E_i. \quad (26)$$

A measure for the cellular binding strength can be derived from the sum of all binding energies with the next neighbors

$$\Sigma_i(t) = \sum_{j \in \mathcal{NN}(i)} \sigma_{ij}(t) A_{ij}(t). \quad (27)$$

Assuming that cells with low binding are shed off from the skin surface, we remove necrotic and cornified cells from the simulation as soon as their binding strength falls below a critical value  $\Sigma_i \leq \Sigma^{\min}$  (model parameter). Note that this choice also has the consequence that non-viable cells without contact to other cells are also removed from the simulation. These cells do not have anchorage and would be shed off in the realistic epidermis. Though the loss of receptors and ligands as well as decreasing cell elasticity may be reasonable assumptions for cornified and necrotic

cells, the overall time course may be quite different in reality. We have tried other forms of necrotic cell removal. For example, one could think of removing non-viable cells randomly at a constant rate as was done in [13]. This possibility however did significantly disturb the layered structure of the *stratum corneum*. Holes in this protective layer in turn did lead to sudden loss of water in the epidermis and thereby to irregular proliferative behavior and considerable oscillations in epidermal thickness. The same problem occurred when assuming a (Gaussian-distributed) cell-specific eigentime after which non-viable cells were removed from the simulation.

The stochastic elements involved in the cell cycle dynamics are the initial direction of mitosis and the durations of the M-phase, the S/G<sub>2</sub>-phase, and the G<sub>0</sub>-phase. It is an empirical fact that times observed in biological systems underly significant stochastic deviations: For example, cell populations starting from a single cell desynchronize proliferation after about five generations [50]. This behavior can not be explained by processes such as contact inhibition or nutrient depletion, as these are not active for small systems with only 2<sup>5</sup> cells. Therefore, these stochastic elements have been included in the M-phase and the S/G<sub>2</sub>-phase. If no stochastic deviation for the G<sub>0</sub>-phase is used, the model exhibits artificial oscillations around a steady state even in later stages.

#### IV. SIMULATION SETUP

As the computational domain, a rectangular box of dimensions 200  $\mu\text{m} \times 200 \mu\text{m} \times 400 \mu\text{m}$  has been considered. As outlined in section II, epidermal tissue is obviously anisotropic. Thus, the boundary conditions are non-homogeneous as well. Since the cellular kinetics is described with a system of ordinary differential equations ( 22), the term “boundary condition” refers to the special interactions at the boundary of the computational domain. It is known that a realistic epidermis exhibits a ruffled basal layer [15]. In order to treat the microenvironment of epidermal tissue as simple as possible, the basal layer has been implemented here as a static planar boundary at the bottom with normal vector  $e_z$ . With using the JKR model ( 4), such a planar boundary can be well implemented by assuming contact with a cell of infinitely large radius. In addition, the  $z$ -boundary has been assumed to be of infinite elasticity  $E_{\text{bound}} = \infty$ . Since the elastic parameters enter additively in equation ( 2), this choice does not sensitively change the global model behavior but merely shifts the equilibrium distance between basal membrane and bottom cell layer. The corresponding adhesive anchorage in the basal layer has been made dependent on the cell type. In order to minimize the boundary effects in  $x$  and  $y$  direction, periodic boundary conditions could be used. This however would necessitate a rather tedious mirroring of cells close to the boundary. Therefore, here a different (mirror cell) approach has been chosen: Every cell in contact with a  $x$  or  $y$  boundary is assumed to be in contact with a cell of similar type, size, receptor and ligand equipment, etc. In short, it interacts with a virtual mirror copy of itself, where the contact area is situated within the boundary plane. In upper  $z$ -direction there are no boundary conditions on the cells – recall that necrotic or cornified cells are removed eventually. Note that in comparison to a static boundary this procedure also has the advantage that drag force artifacts are reduced.

To model the supply with water and nutrients from sub-basal layers, for the diffusion of water and nutrients, the concentration at the lower  $z$ -boundary has been fixed to the maximum value (Dirichlet boundary conditions), and above the cell layers (dynamic thickness, a *stratum corneum* need not always exist during the simulations) both concentrations are fixed to 0. Technically, this has been implemented by setting the concentrations to vanish at all grid volume elements not containing any cells. The resolution of the reaction-diffusion grid was low enough to prevent the emergence of artificial sink terms in intercellular cavities throughout all simulations. At the  $x$  and  $y$  boundaries, no-flux von Neumann boundary conditions have been used, i. e.,  $\partial_x u = 0$  and  $\partial_y u = 0$ . Thus, for an in  $x$  and  $y$  directions homogeneous cell distribution, the problem would effectively reduce to a one-dimensional one.

The initial conditions have been determined as follows: A monolayer of keratinocyte stemcells is distributed on the basal membrane. In addition, at a defined position one (initially non-proliferating) melanocyte is added. Afterwards, the position of the cells in the cell cycle is randomized uniformly to avoid initial artifacts. This configuration could for example mimic a severely perturbed epidermis, where suddenly not only the *stratum corneum* but also the *stratum medium* was removed. Consequently, a strong proliferative response should be expected.

After establishment of a steady-state flow equilibrium, different perturbations have been performed. These include removal of all cornified cells (tape-stripping experiments) and changes in the melanocyte properties and will be discussed in the next section.

## V. RESULTS

### A. Flow equilibrium

Our first question was whether the proposed control mechanism of the water-concentration-induced prolongation of the cell cycle time could actually produce the macroscopically observed flow equilibrium of skin. In particular, we asked whether

- a steady-state flow equilibrium is established, and
- whether this equilibrium is stable against perturbations such as complete removal of the *stratum corneum* that is performed for example in tape-stripping experiments [18].

It turns out that both questions have an affirmative answer (see figure 5). Starting from a monolayer of cells, the

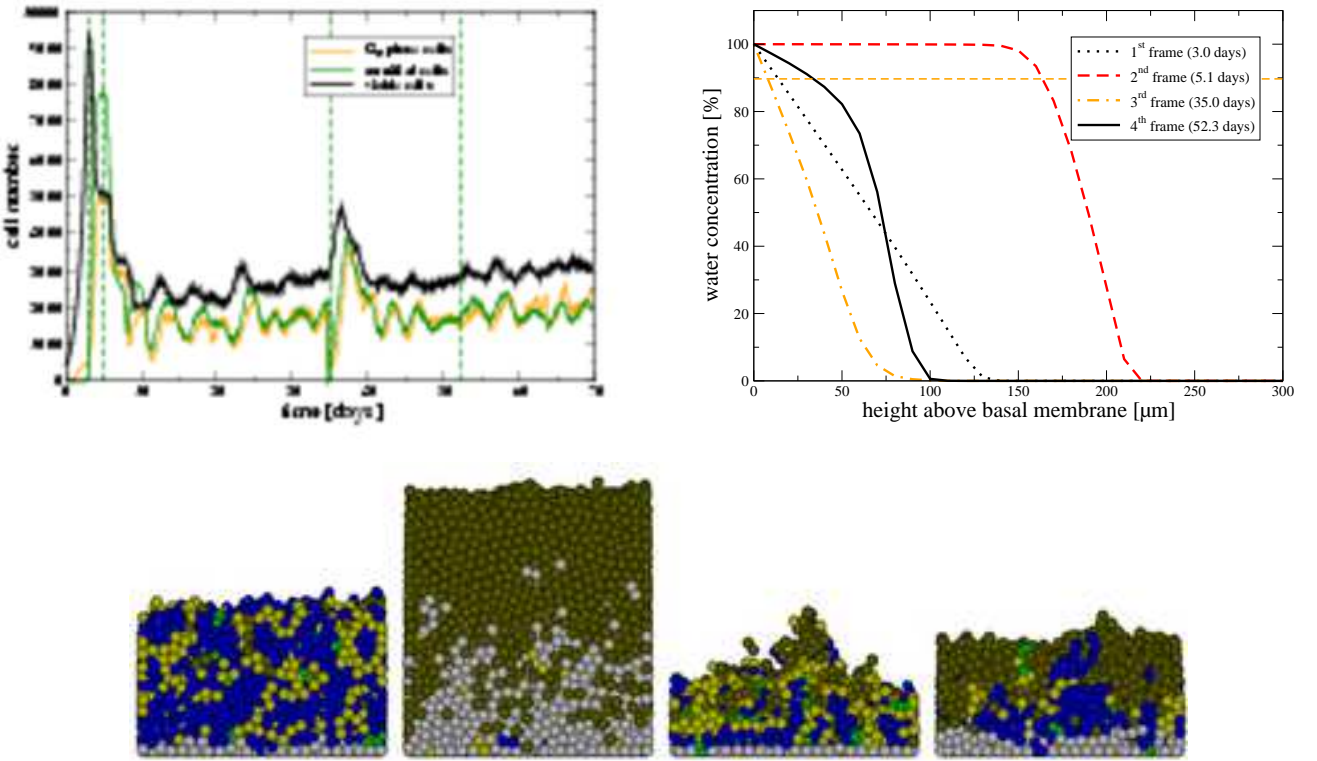


FIG. 5: Emergence of an epidermal steady-state flow equilibrium. **Top Left:** Distribution of keratinocytes in the cell cycle. Cell numbers refer to a ground surface of  $200 \times 200 \mu\text{m}^2$ . Vertical dashed lines indicate times where cross-sections of the keratinocyte distribution (bottom row) and the water concentration (top right) have been extracted. **Top Right:** Shown is the (in  $x$  and  $y$  averaged) dependence of the water concentration on the distance from the basal layer at different times. The maximum value of 100 % correspond to the concentration at the basal membrane and the horizontal dashed line denotes the critical water concentration  $U_{\text{H}_2\text{O}}^{\text{crit}} = 90\%$ . **Bottom row:** Shown is a cross-section of the *in silico* epidermis. Cells in G<sub>0</sub>-phase are marked in light grey, cornified keratinocytes are marked in grey, and darker shades of grey denote the different phases of the cell cycle. The first frame corresponds to an excited state already, whereas the last frame displays the flow equilibrium distribution predicting an approximate thickness of  $120 \mu\text{m}$  above the basal membrane.

local water concentration above the basal membrane is quite low such that no cell enters cell cycle prolongation. The net effect is an initial exponential growth phase (top left panel). After four generations, cornification of the first keratinocytes begins, followed by the formation of a *stratum corneum* with a considerably decreased diffusion coefficient for water. This in turn leads to an increased water concentration and thereby a greater fraction of cells residing in G<sub>0</sub>-phase: The initial exponential growth slows down to polynomial and then decreases, since the cornified cells shed of the skins surface. Afterwards, the dynamics equilibrates. After 35 days, a tape-stripping experiment

has been performed: All cornified cells are suddenly removed from the simulation. This leads again to a proliferative response. However, since this time the cornified layer quickly re-establishes due to reservoir cells in G<sub>0</sub>-phase, the proliferative response is considerably smaller than initially. Note that the dominant contribution to the rapid formation of the cornified layer in the model results from the fraction of G<sub>0</sub>-keratinocytes that have already reached their fourth generation. Interestingly, the oscillations around the equilibrium value are remarkably strong. The number of cells displays a slight (but decelerating) upward tendency, but 15 days after the disturbance (last vertical line), saturation is nearly reached. The final cell numbers correspond well to observed densities of keratinocytes (75000 cells per square mm skin [17]). In the top right panel of figure 5 it is demonstrated that with an intact *stratum corneum* (second and last frame), the water concentration is large in the lower layers of the epidermis and then falls rapidly. In figure 5 bottom row it becomes visible in the latest frame that the cornified layer exhibits a small hole (cells in dark grey). Due to a considerable loss of water, this causes many distant keratinocytes to leave their cell cycle arrest (cells in light grey changing to cells in dark grey) and thereby leads to a perturbation of the equilibrium.

In [47] the authors hypothesize about a diffusible substance that moderates cellular proliferation times. The present model does not contradict the hypothesis that this substance could simply be the moisture of the epidermis but other diffusible substances would presumably lead to equivalent model behavior.

## B. Melanocyte anchorage

Our second question was how the degree of anchorage to the basal layer would influence the ability of cancerous melanocytes to persist within the skin. It is well-known that most human melanoma cell lines have decreased or no expression of cadherins and exhibit a decreased ability to adhere to keratinocytes [51]. At first, we suspected that increased basal adhesion would lead to an increased fraction of melanocytes bound to the basal membrane and thereby a smaller fraction that is shed to regions where the nutrient supply falls below necrosis-inducing levels. Thus, the total number of melanocytes should decrease with decreasing anchorage. In order to test this, a single non-proliferating melanocyte was placed at the basal layer in the center of the computational domain, and the system was evolved until flow equilibrium was established. Then, the melanocyte was turned cancerous by suddenly allowing for proliferation with a much larger rate than keratinocytes. In addition, we concomitantly reduced the anchorage to the basal layer. Starting from experience with multicellular tumor spheroids [13], we assumed the cycle time of cancerous melanocytes to be in the order of 15 hours. Surprisingly, it turned out that with this cycle time for melanocytes and the turnover time estimated for the stemcells in the basal layer, the overall growth dynamics was hardly dependent on the anchorage to the basal layer, see figure 6 left panel. Initially, the growth of melanocytes follows an exponential growth, which is soon slowed down since the melanocytes reach distant regions from the basal layer, where nutrient support is poor. Since due to nutrient depletion the total number of viable cells already indicates saturation, also the total number of melanocytes must saturate eventually. Even with no adhesion to the basal membrane, comparable numbers of tumor cells were achieved. Direct observation of the cross-sections (not shown) revealed the reason: With the given melanocyte proliferation rate of 15 hours, exponential growth was always faster than the epidermal flow induced by the turnover on the basal layer.

Consequently, we varied the proliferation rate of the cancerous cells in combination with complete loss of basal membrane anchorage (see figure 6 right panel). It turned out that there is a region of proliferation rates, where the melanocytes do not persist within the epidermis. This region is separated from the region of melanoma persistence by a comparably large domain where stochastic effects become important. Interestingly, in this case the period of coexistence of healthy skin and transformed cells may be remarkably long, which may give time for further malignant transformations in the realistic epidermis.

We further examined the region that separates melanoma persistence and complete shed-off of cancerous melanocytes by changing the melanocyte cycle time to  $\tau_{\text{mel}} = (44.44 \pm 5.56)$  h. One finds that the usual spherical form one observes for *in vitro* tumor spheroids is considerably deformed for this system to cylinder-shaped or cone-shaped, compare figure 7 left panel. This is due to the pre-existent flow-equilibrium of the surrounding tissue and the effective one-dimensional diffusional constraint. Note also that the boundaries of the tumors are rather diffuse. Initially, a thin column of cancerous melanocytes is formed. Then, in the example in figure 7, left panel, first row, the melanocytes can persist within the life-sustaining zone until their growth velocity outweighs the upward-directed flow velocity and direct contact with the basal membrane is re-established. Afterwards, in the middle of the column of cancerous cells the upward forces are decreased, since for the interior cells there is no direct contact with keratinocytes moving upwards. In the simulations in figure 7 left panel, the thickness of the epidermis increases in those simulations where the tumor has re-established contact with the basal membrane. This is due to the displacement of keratinocytes – which are constrained in *x* and *y* dimensions – and also to the loss of the protective cornified layer, which leads to enlarged keratinocyte proliferation rates. It may be speculated that the cross-sections correspond to initial stages of a highly aggressive nodular melanoma [19] that has not yet become clinically manifest. It may be hypothesized that

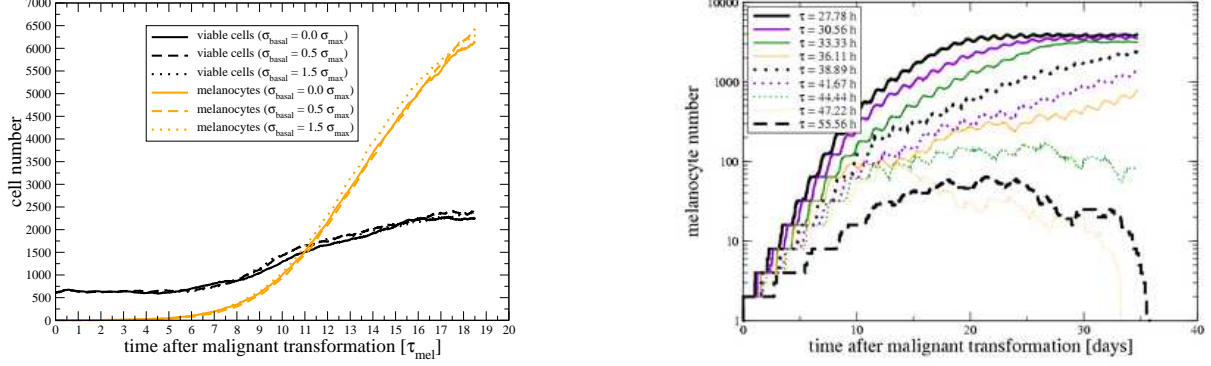


FIG. 6: **Left:** Total number of melanocytes (grey, including necrotic and viable melanocytes) and viable cells (black, including stemcells, keratinocytes, and melanocytes) for different degrees of basal adhesion versus time – expressed in units of the cancerous melanocyte cycle time. For the assumed melanocyte cycle time of  $\tau_{\text{mel}} = (15.0 \pm 2.0)$  h and other parameters chosen as in table I, the basal anchorage has no significant effect on the overall dynamics. **Right:** With considerably slower melanocyte proliferation and completely absent adhesion to the basal layer, a parameter regime can be found where melanoma do not persist within the steady-state flow equilibrium. There, the system is sensitive to stochastic effects, as is also indicated in the disturbed order (some curves intersect). The slowly-damped oscillations stem from the small standard deviations of cell cycle durations (2 h in every run).

the micrometastases sometimes observed around primary melanoma in skin may correspond to branches of melanoma clones that have separated from the main clone during the upward flow. Interestingly, the shapes of these structures appear to be dynamically changing in these initial phases.

Using different initial seed values for the random number generator, we have performed several simulations with otherwise equal parameters. It turns out that completely different outcomes may occur in this region of melanocyte proliferation rates (figure 7 left panel and thick curves in the right panel). The stochastic effects result from stochastic forces, the randomly chosen mitotic direction, and the randomly distributed duration times of the cell cycle. In this *in silico* experiment, the different seed value did already lead to different configurations before the malignant transformation. More specific, the initial conditions for the growth of cancerous melanocytes had also been varied by employing stochastic elements before. In order to separate these effects, we started another series of simulations with equal initial seed values. However, here in contrast the seed value of the random number generators was reset right at the time of the malignant transformation. Thus, the initial environment of the cancerous melanocyte was very similar in these simulations. It turned out that the variance of the outcomes narrowed considerably (thin grey curves in figure 7 right panel) but still exhibit large variations in the cell number (logarithmic plot). Thus, it can be concluded that the initial environment of cancerous melanocytes contributes significantly to the final outcome. Note that this does not only refer to the spatial cellular position, but also to the local proliferative state and thereby to the local upward flow velocity: The upward drag forces will be larger if the cancerous cell is surrounded by many proliferating keratinocytes with a net upward flow velocity.

In conclusion, stochastic effects generally play an important role in the initial phases of *in silico* melanoma development, since for the small cell numbers in the initial phases, they do not average out completely. In addition, their secondary consequences, i. e., the variation of the initial local environment by stochastic influences, are relevant.

## VI. MODEL PARAMETERS

Reasonable dynamics has been achieved with the parameters in table I.

The viscosity of the extracellular matrix  $\eta$  determines the friction on loosely bound cells and – since friction due to the cytoskeleton is assumed to be small ( $\gamma_{\perp} \approx 0$ ) – also dominates friction in directions normal to the cell contact surfaces. Thereby, also the initial speed of cell division in M-phase is dominantly dependent on  $\eta$ . Large viscosities lead to increased friction. As long as the force relaxation occurs on a shorter timescale than the total cell doubling time, this does not have macroscopic effects on the evolution of the tissue. This is different when  $\gamma_{\perp}$  does not vanish. If it has the same order of magnitude as  $\gamma_{\parallel}$ , it will dominate the contribution inflicted by the viscosity  $\eta$ . However, if the magnitude of the total drag force coefficient does not change (marked by  $\gamma^2 = \gamma_{\perp}^2 + \gamma_{\parallel}^2$ , we have found by comparing

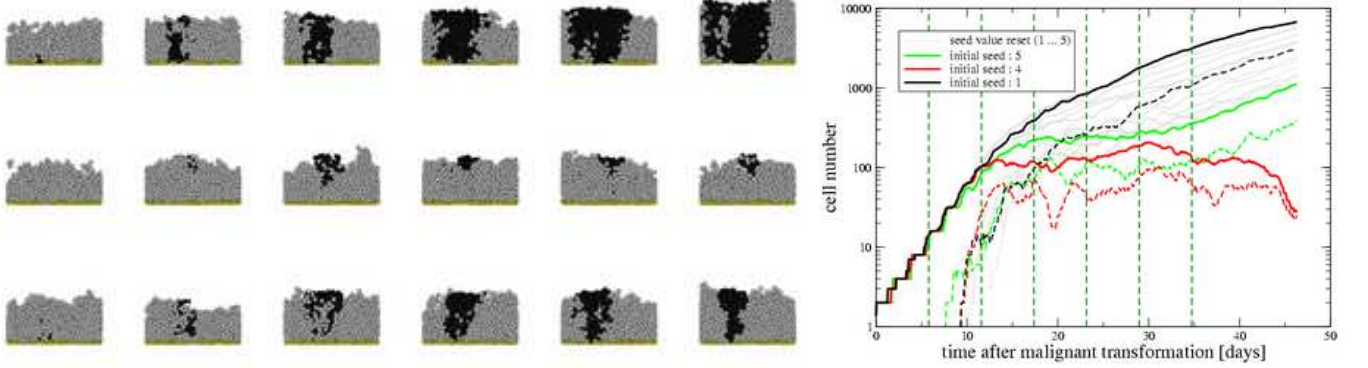


FIG. 7: **Left:** *In silico* evolution of cancerous melanocytes (black) within an epidermal population containing keratinocytes (light grey) and stemcells (the bottom layer). Note that the cross-sections do not distinguish between viable and necrotic or viable and cornified cells, respectively. The times at which the cross-sections have been produced are marked in the right panel with dashed lines. The first row corresponds to the seed value 1 (thick black curves in the right panel), the second row to seed value 4 (thick curves in grey), and the last row to seed value 5 (thick curves in light grey). Note that the diameter of a single frame is  $200 \mu\text{m}$  only, such that the figure represents the state before clinical manifestation. **Right:** Total number of melanocytes (thick lines) and necrotic melanocyte subpopulation (associated dashed curves emerging around day 10) after the malignant transformation. For the thick lines, the different shades of grey correspond to different initial seed values (with otherwise equal parameters) of the random number generator. Consequently, these simulations also already include a changed environment for the melanocyte at the time of its malignant transformation. Note that for seed value 4 there are hardly any viable melanocytes left after 45 days (dashed and solid curves combine). This is different if the stochastic effects do not refer to the initial environment configuration of the cancerous melanocyte (thin curves in light grey).

the three extreme cases (that is,  $\gamma_{\perp} = 0, \gamma_{\parallel} = \gamma$  and  $\gamma_{\perp} = \gamma, \gamma_{\parallel} = 0$  and  $\gamma_{\perp} = \gamma_{\parallel} = \gamma/\sqrt{2}$ ) that the differences in the overall population dynamics are rather small. It may be speculated that this is because in the present calculations the relaxation speed has no direct back-reaction on the number of cells, as in contrast to [13, 41] contact inhibition does not play a role. As here absence of perpendicular friction has been assumed, the tangential friction coefficient  $\gamma_{\parallel}$  dominantly determines the speed of relaxation within the tissue. The chosen value led to reasonable dynamics and has been estimated from [41].

The adhesion energy density  $\sigma^{\max}$  determines the cell-cell equilibrium distance and the binding strength, which was a marker for the removal of necrotic or cornified cells. Generally, this value will in reality be time-dependent, compare also the discussion at the end of subsection III A. Therefore, the binding energy density has been derived from the observed equilibrium distance [34] solving ( 4) instead. With this procedure, the equilibrium distances are in a physiological regime. Note that larger adhesion will lead to smaller equilibrium distances (with moderately increased contact surfaces and drag forces) but also to longer persistence times of dead cells, which results in an increased thickness of the *stratum corneum*. However, due to equation ( 25) this latter effect only enters logarithmically. When both the adhesion energy  $\sigma^{\max}$  and the minimum anchorage  $\Sigma^{\min}$  are decreased, one will still have to decrease the maximum stepsize in the numerical solution to maintain the level of accuracy. This is due to the fact that for decreased adhesion, the equilibrium distance and the contact distance  $d_{ij}^{\text{contact}} = R_i + R_j$  are closer together.

The elastic parameters correspond to approximate physiologic values for cells [41, 53, 54]. However, it is known that – depending on the cell type – significant deviations may occur. With the given drag forces, mechanical relaxation occurs on a shorter scale than the cell cycle times, such that changes in physiologic windows have only small macroscopic consequences. It should be noted however that already for moderately changed Young moduli (and/or reduced Poisson moduli) the equilibrium distance between cells will be shifted, which might make decreased maximum spatial stepsizes necessary in the numerical solution to avoid unphysiological losses of contact.

As has already been discussed above, the stochastic elements may have significant influence on melanoma development. These can be divided into stochastic forces, randomly chosen durations of the cell cycle phases, and the random direction of mitosis.

Stochastic forces contribute to the detachment of cornified and necrotic cells, since these do neither advance in the cell cycle nor proliferate. We have found that small variations in the strength of stochastic forces in physiologic regimes only change the fluctuations in the epidermal thickness around the unchanged equilibrium value. On a technical level, the existence of a planar basal layer in combination with completely absent stochastic forces sometimes led to planar cell configurations at the basal layer, which is unfavorable for the Delaunay triangulation [42]. As may be expected,

parameter	value	comment
ECM viscosity $\eta$	0.001 kg/(\mu m s)	[13, 41]
adhesion energy density $\sigma^{\max}$	0.0001 Nm/m <sup>2</sup>	[34]
minimum anchorage $\Sigma^{\min}$	0.00001 pJ	estimate
receptor loss rate $\alpha$	0.00001/s	estimate
tangential friction coefficient $\gamma_{\parallel}$	0.1 · 10 <sup>12</sup> Ns/m <sup>3</sup>	[41]
stochastic force coefficient $\xi$	0.001 · 10 <sup>-6</sup> kg m/s <sup>3/2</sup>	$D = 0.0001 \mu\text{m}^2/\text{s}$ [13, 41]
M-phase duration $\tau^{(m)}$	(1.0 ± 0.25) h	[13]
S/G <sub>2</sub> -phase duration $\tau^{(S/G_2)}$	(5.0 ± 2.0) h	[13]
keratinocyte G <sub>0</sub> -phase prolongation $\tau^{(G_0)}$	(138.9 ± 138.9) h	[18]
shortest observed keratinocyte cycle time $\tau^{\min}$	15 h	[13, 18]
pre-mitotic cell radius $R^{(m)}$	5.0 μm	[52]
cell elastic modulus $E_i$	750 Pa	[53]
cell Poisson ratio $\nu_i$	1/3	[54]
melanocyte glucose uptake rate $\lambda^{(mel)}$	150.0 amol/(cell s)	[55]
keratinocyte glucose uptake rate $\lambda^{(ker)}$	10.0 amol/(cell s)	estimate
critical water concentration $U_{H_2O}^{\text{crit}}$	90.0 %	[49]
maximum water concentration $U_{H_2O}^{\text{bound}}$	100.0 %	by definition
critical glucose concentration $U_{\text{gluc}}^{\text{crit}}$	1.0 mM	[56]
water diffusivity $D_{H_2O}^{\text{strat.med.}}$	1000.0 μm <sup>2</sup> /s	[57, 58]
water diffusivity $D_{H_2O}^{\text{strat.corn.}}$	0.2 μm <sup>2</sup> /s	[48, 59]
glucose diffusivity $D_{\text{gluc}}^{\text{tissue}}$	256.0 μm <sup>2</sup> /s	[60]
glucose boundary concentration $U_{\text{gluc}}^{\text{bound}}$	5.0 mM	[61]
stemcell basal adhesion energy density $\sigma^{\text{basal}}$	$2\sigma^{\max}$	estimate

TABLE I: Model parameters have been estimated from independent experiments or they have been varied as fit parameters. Parameters not included in the table have been varied and are discussed in separate sections of this article.

considerably larger stochastic forces have a strong influence on the thickness of the *stratum corneum*, since loosely bound cells are removed much faster and the protective layer is lost easily. This in turn leads to loss of water and on-going reactions of keratinocytes that leave  $G_0$ -phase.

The values of the durations of M-phase  $\tau^{(m)}$ , the  $S/G_2$ -phase  $\tau^{(S/G_2)}$  and the prolongation of the cell cycle  $\tau^{(G_0)}$  influence the relative distribution of cells within the cell cycle, whereas the sum of their squared widths primarily determines the speed of desynchronization of cell division (compare figures 6 and 7 right panels). Due to missing data, the durations of these cellular states have been fixed from a previous publication [13]. The shortest observed cycle time determines the proliferation time for keratinocytes when the water concentration is below the critical threshold and has been estimated from experimental observations [47]. The system is most sensitive to the  $G_0$ -phase prolongation time  $\tau^{(G_0)}$ , which has been estimated from [18] to yield reasonable dynamics.

Without the modeling constraint that on division of keratinocyte stemcells, only the upper cell becomes a differentiating keratinocyte, the basal layer would loose more and more stemcells in the model. In other cell divisions, the simple assumption of a randomly distributed initial mitotic direction did not lead to numerical artifacts. However, it can be expected that the configuration of the neighbor cells soon changes the initial direction of the mitotic doublet.

The equilibrium thickness of the cornified layer is strongly dependent on the receptor loss rate  $\alpha$  and the minimum anchorage  $\Sigma^{\min}$ . In addition, it will be sensitive to the cycle times of stemcells and keratinocytes, since these determine the number of keratinocytes finally undergoing cornification.

The average cell volume of keratinocytes varies from 425 μm<sup>3</sup> for cornified cells to 800 μm<sup>3</sup> for *stratum granulosum* keratinocytes [52]. Therefore, with the intrinsic assumption of spherical shape, the maximum cell radius has been fixed to  $R^{(m)} = 5.0 \mu\text{m}$ , which also influences the time-dependent target volume. Note however, that within the *stratum corneum* the cornified cells flatten considerably and the realistic intrinsic cell shape cannot be regarded as spherical anymore.

The glucose uptake rate for cancerous melanocytes  $\lambda^{(mel)}$  has been chosen considerably larger than the glucose uptake rate of keratinocytes  $\lambda^{(ker)}$ . This is motivated by the assumption that cancerous cells have a considerably increased metabolism. The actual values are in the range observed for other tumor cells [55]. The minimum nutrient concentration  $U_{\text{gluc}}^{\text{crit}}$ , below which for melanocytes necrosis is induced, has been chosen to be in the order of 1 mM, since necrosis of cancer cells becomes visible at these nutrient concentrations *in vitro* [56, 62]. Thereby, the combination of melanocyte nutrient uptake rate and minimum glucose concentration define a region, where melanocytes can survive.

For simplicity we have assumed that as a net effect the cells do not consume or secrete water. The critical relative water concentration  $U_{H_2O}^{\text{crit}}$  has been adjusted to obtain a reasonable equilibrium thickness of the *stratum medium* with

$\mathcal{O}(5)$  cell layers.

The apparent water diffusivity  $D_{\text{H}_2\text{O}}^{\text{strat.med.}}$  in *stratum medium* as well as in *stratum corneum*  $D_{\text{H}_2\text{O}}^{\text{strat.corn.}}$  has been determined experimentally by various studies. Though strong variances exist, all of them predict a strong decline of the apparent diffusion coefficient [48, 49, 59]. Roughly speaking, the local water diffusion coefficients influence the gradient of water concentration: Large diffusion coefficients correspond to a small gradient. Therefore, for an intact *stratum corneum* the water concentration is approximately constant throughout the *stratum medium* and then falls rapidly, compare also figure 5 right panel.

The same general features hold true for the glucose diffusion coefficient  $D_{\text{gluc}}^{\text{tissue}}$ , which has specifically been determined for the human skin [60]. The glucose concentration at the basal layer  $U_{\text{gluc}}^{\text{bound}}$  has been fixed to values that are normal for blood [61] for non-diabetic persons. However, it should be noted that in reality the blood glucose concentration may vary significantly – for example after a meal. Since within the model for normal parameter sets anoikis is the predominant pathway for keratinocytes and dominantly the cancerous melanocytes consume glucose at large rates in the model, the glucose concentration strongly influences the chances of melanocyte survival here.

In order not to loose stemcells at the basal layer migrating upwards to the *stratum corneum*, the basal adhesion energy has been chosen to be twice the maximum adhesion energy density  $\sigma^{\max}$ . This did suffice to disable loss of stemcells. For non-proliferating melanocytes, the basal adhesion has been chosen similarly.

## VII. DISCUSSION

It had been demonstrated in [13] that with the aid of kinetic and dynamic weighted Delaunay triangulations agent-based models can treat up to  $10^5 \dots 10^6$  cells. In the present contribution, it has been shown that with a more complete treatment of the equations of motion, such models can still handle  $10^4 \dots 10^5$  cells. From a biological point of view, a diffusible substance can serve as a moderator on cellular proliferation in the epithelium. The parameters used suggest that a simple candidate of this substance could be extracellular water. The homeostasis was found to be stable against perturbations such as tape-stripping experiments. Independently, the consequences of a varying basal adhesion of cancerous melanocytes have been studied. It turned out that these are strongly interlinked with the balance of proliferative melanocyte and keratinocyte activities. In addition, it has been shown that in some regions of parameter space, stochastic effects and especially their consequences on the initial state on the environment play an important role in the *in silico* representation of melanoma growth. It is the truth content of some critical assumptions and the quality of the applied approximations that determine the applicability of these results to reality. The model presented has some shortcomings, which we summarize below:

From our point of view, the most significant macroscopic shortcoming of our approach is the failure of the model to explain the reduced thickness of the *stratum corneum*. This is due to the fact that the inherent cell shape is spherical, whereas cornified cells flatten and form polarized adhesive bindings [15]. In reality, this will lead to a greater stability of the *stratum corneum* in comparison to the model, which would also imply a smoother evolution around the steady-state flow equilibrium than exhibited in figure 5 left panel. Possibly, choosing ellipsoids in contrast to spheres as the intrinsic cell shape [12] may provide an alternative. Another possibility would be to use boundary-based models such as e. g. the extended Potts model [63], which however should be carefully adapted to cellular processes and has the disadvantage of using enormous computational resources due to the many degrees of freedom.

From the theoretical point of view, the model could be significantly improved by deriving a contact model valid for two-body interactions that also include non-normal forces and do not underlie the constraints of only small cell deformations. Also, for *in vitro* cell populations that are not fixed to a substrate, the effects of torque may become important. These refined theories however require much better experimental resolution than currently provided. It appears questionable whether center-based models are able to cope with the increasing degree of complexity resulting from these improvements.

The basal layer has been approximated with a plane boundary condition in this article. In reality however, this basal layer is known to have a corrugated structure. This would significantly enlarge the region where water and nutrients are provided in abundance and thereby lead to a far greater cell reservoir that is able to start a proliferative response in case of injury. It may be speculated that this is one of the reasons why the ruffled basal layer has developed in skin.

The dynamics of the nutrients and of water has been described with a reaction-diffusion approach here. However, due to the cellular movement, there will also be a convective and a transport contribution that is completely neglected in the current simulations. With the large diffusion coefficient for water and nutrients in viable tissues, this approximation is presumably valid within the viable layers but may be questionable in the *stratum corneum*. Note that the polarized structure of the cornified cells in the *stratum corneum* may also give rise to non-isotropic diffusion, where the diffusion coefficient is not a scalar value anymore. To a first approximation however, this effect may be well absorbed into the apparent diffusion coefficient as is done in the experimental measurements.

The cell cycle has been approximated here by a small number of internal cellular states only. It may also be questioned whether a subdivision into discrete substates makes sense. One may also expect a much smoother reaction of the epidermis to the removal of all keratinocytes if transition into and out of G<sub>0</sub>-phase would not depend on a threshold water concentration, but would be determined by transition probabilities that may continuously depend on the water concentration. This may be judged with quantified experimental data.

The model also uses comparably many parameters but all of them have a distinct physical counterpart. This makes it possible to determine many parameters by independent experiments. Despite of all the previously-mentioned shortcomings (most of these being valid for lattice-based approaches as well), off-lattice agent-based models also have important advantages over most lattice models: They are less vulnerable to artifacts resulting from anisotropies and have the intrinsic potential to use physical (realistic) parameters with a moderate increase in computational effort. This opens the possibility to gain knowledge about the system by falsifying the model using independent experiments. Therefore, quantified experiments on well-defined experimental systems are of urgent interest to constrain the uncontrolled growth in the number of theoretical models on cellular tissue.

## VIII. ACKNOWLEDGMENTS

G. S. is indebted to J. Galle and T. Beyer for valuable discussions on contact models, physiologic parameters, and numerical algorithms.

---

[1] J. D. Murray. Mathematical Biology I, volume 17 of *Interdisciplinary Applied Mathematics*. Springer, Berlin Heidelberg, 3<sup>rd</sup> edition, 2002.

[2] E. Bettelheim, O. Agam, and N. M. Shnerb. "Quantum phase transitions" in classical nonequilibrium processes. *Physica E* **9**, 600–608, 2001.

[3] R. A. Gatenby and P. K. Maini. *Cancer summed up*. *Nature* **421**, 321–322, 2003.

[4] F. Graner and J. A. Glazier. *Simulation of Biological Cell Sorting Using a Two-Dimensional Extended Potts Model*. *Physical Review Letters* **69**(13), 2013–2016, 1992.

[5] J. von Neumann. Theory of Self-Reproducing Automata. University of Illinois Press, 1<sup>st</sup> edition, 1966.

[6] S. Dormann and A. Deutsch. *Modeling of self-organized avascular tumor growth with a hybrid cellular automaton*. *In Silico Biology* **2**(3), 393–406, 2002.

[7] F. Meineke, C. Potten, and M. Loeffler. *Cell migration and organization in the intestinal crypt using a lattice-free model*. *Cell Proliferation* **34**, 253–266, 2001.

[8] M. Meyer-Hermann and P. K. Maini. *Interpreting two-photon imaging data of lymphocyte motility*. *Physical Review E* 2004. To appear.

[9] M. Weliky and G. Oster. *The mechanical basis of cell rearrangement*. *Development* **109**, 373–386, 1990.

[10] M. Weliky, G. Oster, S. Minsuk, and R. Keller. *Notochord morphogenesis in Xenopus laevis: Simulation of cell behavior underlying tissue convergence and extension*. *Development* **113**, 1231–1244, 1991.

[11] D. Drasdo, R. Kree, and J. S. McCaskill. *Monte Carlo approach to tissue-cell populations*. *Physical Review E* **52**(6), 6635–6657, 1995.

[12] J. Dallon and H. G. Othmer. *How cellular movement determines the collective force generated by the Dictyostelium discoideum slug*. *Journal of Theoretical Biology* **231**(2), 203–222, 2004.

[13] G. Schaller and M. Meyer-Hermann. *Multicellular Tumor Spheroid in an off-lattice Voronoi/Delaunay cell model*. *Physical Review E* **71**, 051910–16, 2005.

[14] G. Schaller and M. Meyer-Hermann. *Continuum versus Discrete model: A Comparison for Multicellular Tumour Spheroids*. submitted to Philosophical Transactions of the Royal Society 2005.

[15] W. Montagna, A. M. Kligman, and K. S. Charlisle. *Atlas of Normal Human Skin*. Springer Verlag, New York, 1992.

[16] S. B. Hoath and D. G. Leahy. *The organization of Human epidermis: Functional Epidermal Units and Phi Proportionality*. *The Journal of Investigative Dermatology* **121**(6), 1440–1446, 2003.

[17] J. Bauer, F. A. Bahmer, J. Wörl, W. Neuhuber, G. Schuler, and M. Fartasch. *A Strikingly Constant Ratio Exists Between Langerhans Cells and Other Epidermal Cells in Human Skin. A Stereologic Study Using the Optical Disector Method and the Confocal Laser Scanning Microscope*. *The Journal of Investigative Dermatology* **116**(2), 313–318, 2001.

[18] D. Barthel, B. Matthe, C. S. Potten, G. Owen, and M. Loeffler. *Proliferation in murine epidermis after minor mechanical stimulation. Part 2. Alterations in keratinocyte cell cycle fluxes*. *Cell Proliferation* **33**, 247–259, 2000.

[19] M. Moncrieff. The clinical application of spectrophotometric intracutaneous analysis for the diagnosis of cutaneous malignant melanoma. Ph.D. thesis, University of East Anglia, 2001.

[20] A. Rahman. *Correlations in the Motion of Atoms in Liquid Argon*. *Physical Review* **136**, A405–A411, 1964.

[21] J.-A. Ferrez. Dynamic triangulations for efficient 3d simulations of granular materials. Ph.D. thesis, EPFL, thesis 2432, 2001.

[22] E. Palsson and H. G. Othmer. *A model for individual and collective cell movement in *Dictyostelium discoideum**. Proceedings of the National Academy of Sciences **97**(19), 10448–10453, 2000.

[23] E. Palsson. *A three-dimensional model of cell movement in multicellular systems*. Future Generation Computer Systems **17**, 835–852, 2001.

[24] D. E. Ingber. *Tensegrity I: Cell structure and hierarchical systems biology*. Journal of Cell Science **116**(7), 1157–1173, 2003.

[25] D. E. Ingber. *Tensegrity II: How structural networks influence cellular information processing networks*. Journal of Cell Science **116**(8), 1397–1408, 2003.

[26] K. L. Johnson. *A note on the adhesion of elastic solids*. British Journal of Applied Physics **9**, 199–200, 1958.

[27] K. L. Johnson, K. Kendall, and A. D. Roberts. *Surface Energy and the Contact of Elastic Solids*. Proceedings of the Royal Society of London A **324**(1558), 301–313, 1971.

[28] C. Verdier. *Rheological Properties of Living Materials. From Cells to Tissues*. Journal of Theoretical Medicine **5**(2), 67–91, 2003.

[29] V. T. Moy, Y. Jiao, T. Hillmann, H. Lehmann, and T. Sano. *Adhesion Energy of Receptor-Mediated Interaction Measured by Elastic Deformation*. Biophysical Journal **76**, 1632–1638, 1999.

[30] H. Hertz. *Über die Berührung fester elastischer Körper*. Journal für die reine und angewandte Mathematik **92**, 156–171, 1882.

[31] L. D. Landau and E. M. Lifshitz. *Theory of Elasticity*. Pergamon Press, London, 1959.

[32] N. N. Brilliantov and T. Pöschel. *The Physics of Granular Media*, chapter Collision of viscoelastic particles with adhesion. Wiley-VCH, Berlin, 2004.

[33] M. Benoit, D. Gabriel, G. Gerisch, and H. E. Gaub. *Discrete interactions in cell adhesion measured by single-molecule force spectroscopy*. Nature Cell Biology **2**, 313–317, 2000.

[34] Y.-S. Chu, W. A. Thomas, O. Eder, F. Pincet, E. Perez, J. P. Thiery, et al. *Force measurements in E-cadherin-mediated cell doublets reveal rapid adhesion strengthened by actin cytoskeleton remodeling through Rac and Cdc42*. Journal of Cell Biology **167**(6), 1183–1194, 2004.

[35] H. Edelsbrunner and N. Shah. *Incremental Topological Flipping Works for Regular Triangulations*. Algorithmica **15**, 223–241, 1996.

[36] J. Galle, G. Aust, G. Schaller, T. Beyer, and D. Drasdo. *Individual cell-based models of the spatio-temporal organisation of multicellular systems – achievements and limitations*. submitted 2005.

[37] D. Drasdo. *Polymer and cell dynamics*, chapter On selected individual-based approaches to the dynamics in multicellular systems, 169–204. Birkhäuser, Basel, 2003.

[38] Q. Ma and J. A. Izaguirre. *Long time step molecular dynamics using targeted Langevin stabilization*. In Proceedings of the 2003 ACM symposium on Applied computing, 178–182. Symposium on Applied Computing, ACM Press, New York, NY, USA, 2003.

[39] B. M. Gammel. *Matpack C++ Numerics and Graphics Library 1.7.3*, 2003.  
<http://www.matpack.de/>.

[40] D. A. Fletcher and J. A. Theriot. *An introduction to cell motility for the physical scientist*. Physical Biology **1**, T1–T10, 2004.

[41] J. Galle, M. Loeffler, and D. Drasdo. *Modeling the Effect of Deregulated Proliferation and Apoptosis on the Growth Dynamics of Epithelial Cell Populations In Vitro*. Biophysical Journal **88**, 62–75, 2005.

[42] G. Schaller and M. Meyer-Hermann. *Kinetic and dynamic Delaunay tetrahedralizations in three dimensions*. Computer Physics Communications **162**, 9–23, 2004.

[43] G. Joos. *Lehrbuch der Theoretischen Physik*. AULA-Verlag, Wiesbaden, 15<sup>th</sup> edition, 1989.

[44] J. R. Shewchuk. *An Introduction to the Conjugate Gradient Method Without the Agonizing Pain*. Technical report, Carnegie Mellon University, Pittsburgh, PA, USA, 1994.

[45] W. H. Press, S. A. Teukolsky, W. T. Vetterling, and B. P. Flannery. *Numerical Recipes in C*. Cambridge University Press, 2<sup>nd</sup> edition, 1994.

[46] N. Gershenfeld. *The Nature of Mathematical Modeling*. Cambridge University Press, Cambridge, 2000.

[47] C. S. Potten, Y. Q. Li, R. Ohlrich, B. Matthe, and M. Loeffler. *Proliferation in murine epidermis after minor mechanical stimulation. Part 1. Sustained increase in keratinocyte production and migration*. Cell Proliferation **33**, 231–246, 2000.

[48] S. J. Bashir, A.-L. Chew, A. Anigbogu, F. Dreher, and H. I. Maibach. *Physical and physiological effects of stratum corneum tape stripping*. Skin Research and Technology **7**, 40–48, 2001.

[49] G. B. Kasting, N. D. Barai, T.-F. Wang, and J. M. Nitsche. *Mobility of Water in Human Stratum Corneum*. Journal of Pharmaceutical Sciences **92**(11), 2326–2340, 2003.

[50] J.-U. Kreft, G. Booth, and J. W. T. Wimpenny. *BacSim, a simulator for individual-based modelling of bacterial colony growth*. Microbiology **144**, 3275–3287, 1998.

[51] A. Tang, M. S. Eller, M. Hara, M. Yaar, S. Hirohashi, and B. A. Gilchrest. *E-cadherin is the major mediator of human melanocyte adhesion to keratinocytes in vitro*. Journal of Cell Science **107**, 983–992, 1994.

[52] L. Norlen and A. Al-Amoudi. *Stratum Corneum Keratin Structure, Function, and Formation: The Cubic Rod-Packing and Membrane Templating Model*. The Journal of Investigative Dermatology **123**, 715–732, 2004.

[53] R. E. Mahaffy, C. K. Shih, F. C. MacKintosh, and J. Käs. *Scanning Probe-Based Frequency-Dependent Microrheology of Polymer Gels and Biological Cells*. Physical Review Letters **85**(4), 880–883, 2000.

[54] A. J. Maniotis, C. S. Chen, and D. E. Ingber. *Demonstration of mechanical connections between integrins, cytoskeletal filaments, and nucleoplasm that stabilize nuclear structure*. Proceedings of the National Academy of Sciences USA **94**,

849–854, 1997.

- [55] J. P. Wehrle, C. E. Ng, K. A. McGovern, N. R. Aiken, D. C. Shungu, E. M. Chance, *et al.* *Metabolism of alternative substrates and the bioenergetic status of EMT6 tumor cell spheroids*. NMR in Biomedicine **13**, 349–460, 2000.
- [56] J. P. Freyer and R. M. Sutherland. *Regulation of Growth Saturation and Development of Necrosis in EMT6/Ro Multicellular Spheroids by the Glucose and Oxygen Supply*. Cancer Research **46**(7), 3504–3512, 1986.
- [57] T. L. Chenevert, J. G. Pipe, D. M. Williams, and J. A. Brunberg. *Quantitative measurement of tissue perfusion and diffusion in vivo*. Magnetic Resonance in Medicine **17**(1), 197–212, 1991.
- [58] E. H. Livingston and E. Engel. *Modeling of the gastric gel mucus layer: application to the measured pH gradient*. Journal of Clinical Gastroenterology **21**, S120–S124, 1995. Suppl. 1.
- [59] D. A. Schwindt, K. P. Wilhelm, and H. I. Maibach. *Water Diffusion Characteristics of Human Stratum Corneum at Different Anatomical Sites in vivo*. The Journal of Investigative Dermatology **111**(3), 385–389, 1998.
- [60] V. V. Tuchin, A. N. Bashkatov, E. A. Genina, Y. P. Simichkin, and N. A. Lakodina. *In vivo Investigation of the immersion-liquid-induced human skin clearing dynamics*. Technical Physics Letters **27**(6), 489–490, 2001.
- [61] G. Carvalho, A. Moore, B. Qizilbash, K. Lachapelle, and T. Schricker. *Maintenance of normoglycemia during cardiac surgery*. Anesthesia and Analgesia **99**(2), 319–324, 2004.
- [62] J. P. Freyer and R. M. Sutherland. *Proliferative and Clonogenic Heterogeneity of Cells from EMT6/Ro Multicellular Spheroids Induced by the Glucose and Oxygen Supply*. Cancer Research **46**(7), 3513–3520, 1986.
- [63] N. J. Savill and J. A. Sherratt. *Control of epidermal stem cell clusters by Notch-mediated lateral induction*. Developmental Biology **258**, 141–153, 2003.